Plate Motions and Stresses from Global Dynamic Models
Attreyee Ghosh*, et al.*
Science **335**, 838 (2012);
DOI: 10.1126/science.1214209

with promoters that limit the hydrogenation reactions (8), thus favoring chain growth and the termination step via β-hydride abstraction that cannot give rise to CH_4 production. The suppression of the methanation reaction induced by the promoters was only observed when using CNF or α-Al_2O_3 because these "inert" supports are thought to favor the proximity between iron and promoters (Na plus S), in contrast to reactive supports such as γ-Al_2O_3 that lead to more methane (Fig. 3). In the case of the bulk catalysts, CH_4 selectivities coincided with the values predicted by the ASF model or were slightly above.

Mössbauer spectroscopy of the spent catalysts after reaction at 1 bar (table S5) showed that the nature of the iron phases varied when using different support materials. Although some of the iron carbides may be oxidized after exposure to air, Fe_xC_y was detected on the samples with moderate to high catalytic activity. In contrast, the samples with the lowest catalytic activity, Fe/SiO_2 and Fe/γ-Al_2O_3, did not contain any carbides. A strong metal-support interaction clearly inhibits the formation of catalytically active iron carbides, as observed for conventional high-surface-area support materials. Note that in the size range of iron particles dispersed on inert supports (7 to 20 nm), particle size effects seem to be minimal.

TEM performed on spent catalysts revealed that the iron nanoparticles in the supported samples increased in size. The particle size distributions of the fresh and spent Fe/α-Al_2O_3 and Fe/CNF are shown in fig. S2. For Fe/CNF, changes in the catalytic activity were only observed during the first 4 hours of reaction, which suggests that the changes in the catalyst structure took place during catalyst activation and initial usage. In the case of Fe/α-Al_2O_3, the average iron nanoparticle size increased from 14 ± 5 nm to 17 ± 5 nm (Fig. 1C). The promoted bulk iron oxide showed

extensive particle fragmentation and carbon filament growth, which brings about the poor mechanical stability of this catalyst (Fig. 1D).

The spent catalysts were characterized with thermogravimetric analysis to determine the extent of carbon lay-down. Carbon burn-off experiments were performed for all the samples, except for the Fe/CNF catalyst. Although extensive carbon deposition on the samples after reaction with CO-rich syngas and high temperatures could be expected, most of the samples exhibited low solid carbon formation. After 64 hours of reaction at 340°C and 20 bar, the levels of carbon lay-down measured on the spent catalysts were lower than 10 wt %. In contrast, Fe/α-Al_2O_3 (25 wt % Fe) and Fe-Cu-K-SiO_2 exhibited a higher extent of coke formation (23 wt % and 40 wt %, respectively).

The FTO process represents a strong alternative route for the sustainable production of lower olefins from biomass-derived synthesis gas. The industrial potential of this process is greatly enhanced by the reported development of active, selective, and mechanically stable catalysts that consist of promoted iron nanoparticles dispersed on weakly interactive supports. Further suppression of methane production, maximization of the C_2-C_4 olefins fraction, and reduction of carbon lay-down by addition of promoters and by optimization of physical properties (e.g., Fe particle size, distribution of Fe nanoparticles on the support) will allow us to further understand and develop the performance of these catalysts.

References and Notes

1. A. Corma, F. V. Melo, L. Sauvanaud, F. Ortega, *Catal. Today* **107–108**, 699 (2005).
2. R. Diercks et al., *Chem. Eng. Technol.* **31**, 631 (2008).
3. S. Wang, Z. H. Zhu, *Energy Fuels* **18**, 1126 (2004).
4. E. L. Kunkes et al., *Science* **322**, 417 (2008).
5. T. P. Vispute, H. Zhang, A. Sanna, R. Xiao, G. W. Huber, *Science* **330**, 1222 (2010).
6. X. Dupain, R. A. Krul, C. J. Schaverien, M. Makkee, J. A. Moulijn, *Appl. Catal. B* **63**, 277 (2006).
7. G. A. Olah, *Angew. Chem. Int. Ed.* **44**, 2636 (2005).
8. C. Wang, L. Xu, Q. Wang, *J. Nat. Gas Chem.* **12**, 10 (2003).
9. B. Büssemeier, C. D. Frohning, G. Horn, W. Kluy, U.S. Patent 4564642 (1986).
10. B. H. Davis, *Catal. Today* **84**, 83 (2003).
11. S. Soled, E. Iglesia, R. A. Fiato, *Catal. Lett.* **7**, 271 (1990).
12. Y. Jin, A. K. Datye, *J. Catal.* **196**, 8 (2000).
13. A. P. Steynberg, M. E. Dry, Eds., *Fischer-Tropsch Technology* (Elsevier, Amsterdam, 2004).
14. M. D. Shroff et al., *J. Catal.* **156**, 185 (1995).
15. J. Barrault, C. Forquy, J. C. Menezo, R. Maurel, *React. Kinet. Catal. Lett.* **15**, 153 (1980).
16. B. G. Baker, N. J. Clark, H. MacArthur, E. Summerville, U.S. Patent 4610975 (1986).
17. D. B. Bukur et al., *Ind. Eng. Chem. Res.* **29**, 1588 (1990).
18. L. Xu, Q. Wang, Y. Xu, J. Huang, *Catal. Lett.* **31**, 253 (1995).
19. M. L. Cubeiro et al., *Appl. Catal. A* **167**, 183 (1998).
20. V. K. Jones, L. R. Neubauer, C. H. Bartholomew, *J. Phys. Chem.* **90**, 4832 (1986).
21. A. P. B. Sommen, F. Stoop, K. van der Wiele, *Appl. Catal.* **14**, 277 (1985).
22. K. P. de Jong, *Oil Gas Sci. Technol.* **61**, 527 (2006).
23. K. P. de Jong, J. W. Geus, *Catal. Rev., Sci. Eng.* **42**, 481 (2000).
24. E. van Steen, F. F. Prinsloo, *Catal. Today* **71**, 327 (2002).
25. W. Chen, Z. Fan, X. Pan, X. Bao, *J. Am. Chem. Soc.* **130**, 9414 (2008).
26. A. J. van Dillen, R. J. A. M. Terörde, D. J. Lensveld, J. W. Geus, K. P. de Jong, *J. Catal.* **216**, 257 (2003).

Plate Motions and Stresses from Global Dynamic Models

Attreyee Ghosh* and William E. Holt

Delineating the driving forces behind plate motions is important for understanding the processes that have shaped Earth throughout its history. However, the accurate prediction of plate motions, boundary-zone deformation, rigidity, and stresses remains a difficult frontier in numerical modeling. We present a global dynamic model that produces a good fit to such parameters by accounting for lateral viscosity variations in the top 200 kilometers of Earth, together with forces associated with topography and lithosphere structure, as well as coupling with mantle flow. The relative importance of shallow structure versus deeper mantle flow varies over Earth's surface. Our model reveals where mantle flow contributes toward driving or resisting plate motions. Furthermore, subducted slabs need not act as strong stress guides to satisfy global observations of plate motions and stress.

Predicting plate motions correctly, along with stresses within the plates, has been a challenge for global dynamic models. Accurate predictions are vitally important for understanding the forces responsible for the movement of plates, mountain building, rifting of continents,

and strain accumulation released in earthquakes. Previous studies have investigated these driving forces by either predicting stresses in the plates alone (1, 2) or plate motions alone (3–5). Other studies have taken the important step of predicting both plate motions and stresses in a single model (6–8). However, in addition to predicting plate motions, a successful global dynamic model must also explain plate rigidity and plate boundary-zone deformation, as well as intraplate stress patterns. Furthermore, the presence of lateral viscosity variations within the top 200 km of Earth influences the coupling between lithosphere and mantle convection. A systematic investigation of this influence is needed to improve our understanding of the driving mechanisms for plate tectonics.

Geosciences Department, Stony Brook University, Stony Brook, NY 11794, USA.

*To whom correspondence should be addressed. E-mail: atreig@gmail.com

We used global dynamic models to investigate the influence of lateral viscosity variations in the lithosphere and asthenosphere on both surface motions and stresses within the plates and plate boundary zones. Our models include incorporation of the effects of topography and lithosphere structure and a lithosphere coupled with whole-mantle convection, driven by density buoyancies within the mantle. Our modeling reveals the lateral viscosity variations that are necessary for matching observations. The results further emphasize the relative contributions of (i) topography and lithosphere structure and (ii) coupling with whole-mantle convection, both of which vary over Earth's surface.

We solved the three-dimensional (3D) force balance equations after depth-integrating them from a surface of variable elevation to a common depth reference level (100 km below sea level) to obtain deviatoric stresses, strain rates, and horizontal velocities within the top 100 km of the planet (9). The body forces in these equations were derived from two sources: (i) topography and lithosphere density structure and (ii) density-driven convection within the mantle constrained by tomography and history of subduction. Benchmarking tests have demonstrated that despite the simplification used in this method, we are able to recover the horizontal components

of stress, strain rate, and velocity in the upper 100 km of a full 3D whole-mantle convection model with better than 99% accuracy (10). We tested different radial and lateral viscosity variations in the lithosphere and asthenosphere, where the lateral variations were assigned based on positions of cratons and weak plate boundary zones (Fig. 1A). A relatively narrow range of viscosity models gave acceptable fits to the observations. Viscosity models that simultaneously gave a good fit to both plate motions and stresses required a stiff lithosphere (10^{23} Pa · s) with stiffer (10^{24} Pa · s) cratons (white regions in Fig. 1A) and weaker plate boundary zones (10^{20} to 10^{22} Pa · s) in the top 100 km and a moderately strong asthenosphere (300-km thickness, 10^{20} Pa · s). The successful models had keels beneath the cratons with viscosities less than 10^{23} Pa · s between depths of 100 to 200 km.

The velocity field predicted by our best-fit dynamic model in a no-net-rotation (NNR) frame shows a remarkably good fit to the NNR plate motion model defined by Global Positioning System (GPS) (Fig. 1B) (11). The root mean square misfit of the velocity field from our complete dynamic model (mantle flow–associated tractions plus lithosphere structure and topography) compared at 63,000 spaced points (1° by 1°) with the kinematic NNR model is ~1 cm/year. The

relative contribution of motions associated with coupling with whole-mantle flow versus topography and lithosphere structure can be understood by inspection of Fig. 1C, which is based on the contribution from mantle circulation tractions only. The relative driving mechanisms of topography and lithosphere structure versus coupling with mantle flow varies from plate to plate. The India and Nazca plates have a dominant influence from coupling with mantle flow, whereas other plates and regions approach parity in the relative contribution, with mantle-flow tractions dominating slightly. It is obvious, however, that the contribution from coupling with mantle circulation alone fails to predict surface motions.

We calculated the poles of rotation (table S1) for the angular velocities of the major tectonic plates that were predicted by the dynamic model and compared them with the latest NNR kinematic model, MORVEL (Fig. 1D) (12). The velocity of any given patch on the surface of our dynamic model was parameterized by an angular velocity possessing a pole position. The small scatter in the pole positions for these patches (blue dots) shows that the plates are behaving almost rigidly at the stress levels output by the dynamic model and for an effective viscosity of the plates of 1×10^{23} Pa · s. A comparison of the
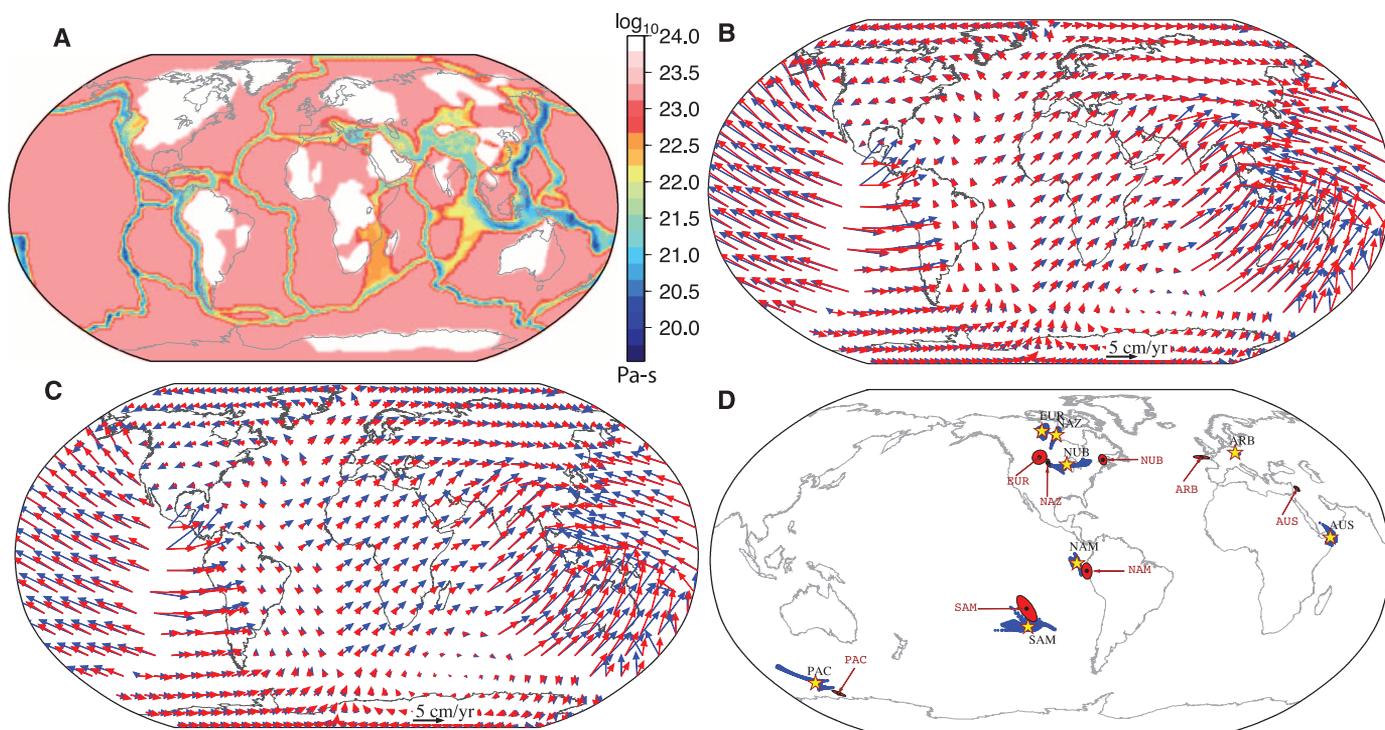

Fig. 1. (A) Absolute viscosity model (top 100 km) that provided a best fit to our observations. **(B)** Kinematic NNR model from (11) (blue arrows), along with predicted velocities from our global dynamic model (red arrows) in an NNR frame. The dynamic model includes contributions from both coupling with whole-mantle convection and lithosphere structure and topography. **(C)** Same as in (B), except the predicted velocities (red arrows) are from mantle tractions only.

(D) Average poles of rotation of major tectonic plates (yellow stars) predicted by the dynamic model on top of individually inferred poles from relatively undeformed patches on the respective plates (blue dots). The NNR MORVEL poles from (12) are shown as black dots within their respective 95% confidence level error ellipses (in red). PAC, Pacific; NAM, North America; SAM, South America; ARB, Arabia; NUB, Nubia; NAZ, Nazca; EUR, Eurasia; and AUS, Australia.

poles of rotation from the NNR MORVEL model (red 95% confidence ellipse) with the average pole positions (yellow stars) shows that the predictions for the North and the South American plates are nearly perfect (Fig. 1D and table S1). The predicted poles of the Pacific, Europe, Nubia, Nazca, and Arabia plates also lie fairly close to the respective poles of the kinematic MORVEL model.

Comparison of relative surface motions provided by our best-fit dynamic model in selected frames of reference with GPS observations (11) shows that the dynamic model is predicting motions in both the plates and plate boundary zones (Fig. 2, A to C). The poles of rotation for the relative angular velocities predicted by the dynamic model (red stars) are, in most cases, close to angular velocities (blue stars) from the latest kinematic plate-motion estimates (13). The gen-

eral agreement of the predicted velocities from the dynamic model to the GPS vectors demonstrates that the model is predicting the correct deformation tensor field within plate boundary zones, including diffuse plate boundary zones, which is a difficult problem for global dynamic models.

Earth's lithospheric stress field gives an indication of the driving forces that cause continental deformation and form mountain ranges and plateaus (1, 14, 15). We compared the orientation and style of our predicted deviatoric stresses with the World Stress Map (WSM) data (16) in the intraplate areas. Our predicted most compressive principal stresses (Fig. 3B) are in good agreement with the WSM horizontal most compressive stress (SH_{max}) directions and style (Fig. 3A). We show the stress results in three important continental deformation zones: western

North America, the India-Asia collision zone, and the central Mediterranean. In western North America, deviatoric stresses from the dynamic model predict the opening of the Basin and Range Province, strike-slip along the San Andreas system, compression within the Juan de Fuca trench, and north-south compression over the Cascadia forearc (Fig. 4A). In the central Mediterranean and eastern Turkey regions, the modeled stresses (Fig. 4B) are compatible with findings of the known deformation field (17). The Hellenic arc displays trench-perpendicular compression, whereas clear strike-slip deformation is predicted along the North Anatolian fault. Improvement in prediction for these continental regions is possible through incorporation of the influence of smaller-scale convection (18). The predicted deviatoric stresses in Tibet show a predominantly strike-slip style of deformation (also mixed with normal fault-

Fig. 2. (**A**) Model velocity vectors (red arrows) from our global dynamic model plotted along with GPS vectors (11) (blue arrows) over North America in a Pacific fixed reference frame. A zoom-in view of the western U.S. region is shown in the inset map. Poles predicted by the dynamic model (red star) and the MORVEL plate-motion model (13) (blue star) are shown for PAC-NAM relative motion. (**B**) Same as in (A), but with Nubia fixed. Poles are for ARB-EUR relative motion. (**C**) Same as in (A), but with India fixed. Poles are for AUS-India relative motion.
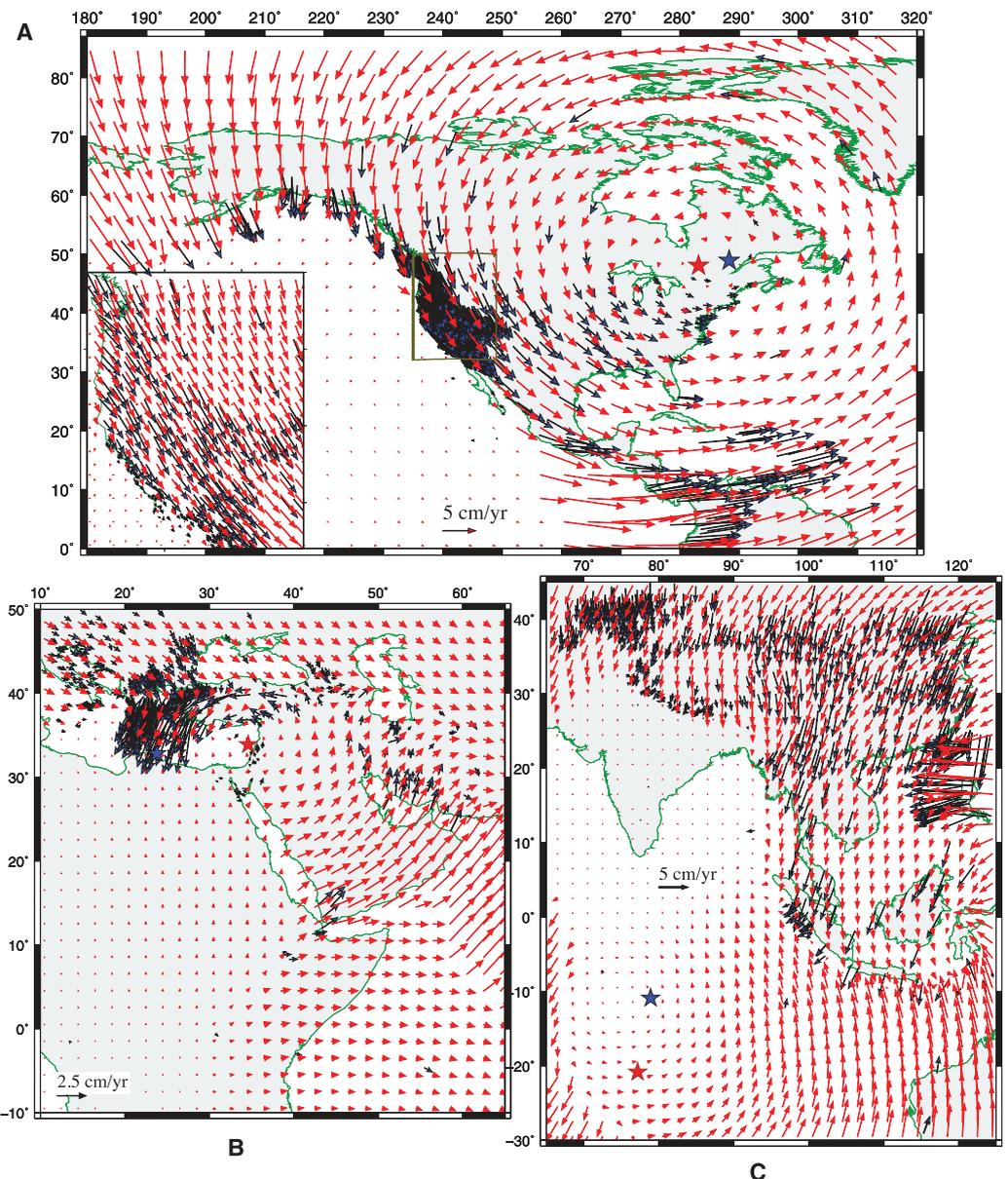
style deviatoric stress) and a rotation of SH_{max} within Tibet around the Eastern Himalayan Syntaxis region (Fig. 4C), similar to what is observed there. The contribution from topography and lithosphere structure plays an important role for these areas of continental deformation. We also compared our predicted stress orientation and style with strain-rate data from the Global Strain Rate Map (GSRM) (19) in the deforming areas by computing a correlation coefficient (20) between the predicted stress tensors and the GSRM strain-rate tensors. The comparison shows a good match in the mid-oceanic ridges, continental Africa and the Indo-Australia oceanic plate boundary zone, as well as in the Andes (fig. S1).

The traction field (21) that contributes to our best-fit dynamic model is long wavelength (Fig. 4D) and shows convergent flow in areas of downgoing slabs and divergent flow in places such as central Africa and the Pacific. Comparison of these tractions with surface velocities (Fig. 1B) indicates whether the tractions are driving or resisting. If mantle flow is leading plate motion, tractions are driving; if mantle flow is trailing the plate, then tractions are resistive. Tractions are driving in

areas like the Nazca plate, eastern North America, the North Atlantic and Western Europe, northern and eastern Siberia, northern Africa, the Indian and Australian plates, and the Pacific plate in regions approaching the subduction zones. In these places, tractions act in similar directions to plate motions in an NNR frame, and thus mantle flow is leading the plate motion. On the other hand, in western North America, the northern part of South America, and southern Africa, tractions are resistive, as they are in a direction opposite to the NNR surface velocity. This is an important conclusion of our study that addresses the hugely controversial issue of whether mantle tractions are driving or resistive (14, 22, 23).

We also calibrated the absolute deviatoric stress magnitudes in the lithosphere verified through benchmarking using whole-mantle convection models (10). The average stress levels (second invariant of deviatoric stresses) within the lithosphere in our best-fit dynamic models are between 20 and 80 MPa (fig. S2). The higher stresses occur within the plates, whereas the plate boundary zones have lower values. At those stress levels, and given the predicted stress and strain-rate tensor fields,

we obtain near-plate rigidity (Fig. 4E) and a close prediction to surface motions. The rigidity of the plates is evident from the low strain rates predicted in the intraplate areas, 1 to 4×10^{-9} per year (white to red areas in Fig. 4E). A goal of this study is to investigate the relative contribution of mantle flow versus lithosphere structure and topography. Although this ratio of the relative contribution varies depending on location, an average of 70% of the magnitude of lithosphere deviatoric stresses is associated with coupling with mantle flow, and the remaining 30% is associated with lithosphere structure and topography.

The issue of whether slabs remain strong (8) or weaken (24–27) as they subduct is still unresolved (28). Our convection model is solely density-driven with Newtonian viscosity; no nonlinear rheology or stiff slabs have been considered, and yet our model predicts global plate motions, as well as motions within most of the world's diffuse plate boundary zones. Our results cannot rule out the need for stiff slabs; we can only infer that they are not a necessary condition for predicting plate motions and plate boundary-zone deformation.

Fig. 3. (**A**) SH_{max} directions from the World Stress Map averaged within 1° by 1° areas. Red indicates a normal fault regime, blue indicates a thrust regime, and green denotes a strike-slip regime. Only SH_{max} directions where the regime was known have been used. (**B**) Most compressive horizontal principal deviatoric stress axes from our best-fitting dynamic model. The colors indicate the strain environment predicted by the deviatoric stresses in the dynamic model. Red, blue, green: same as in (A).
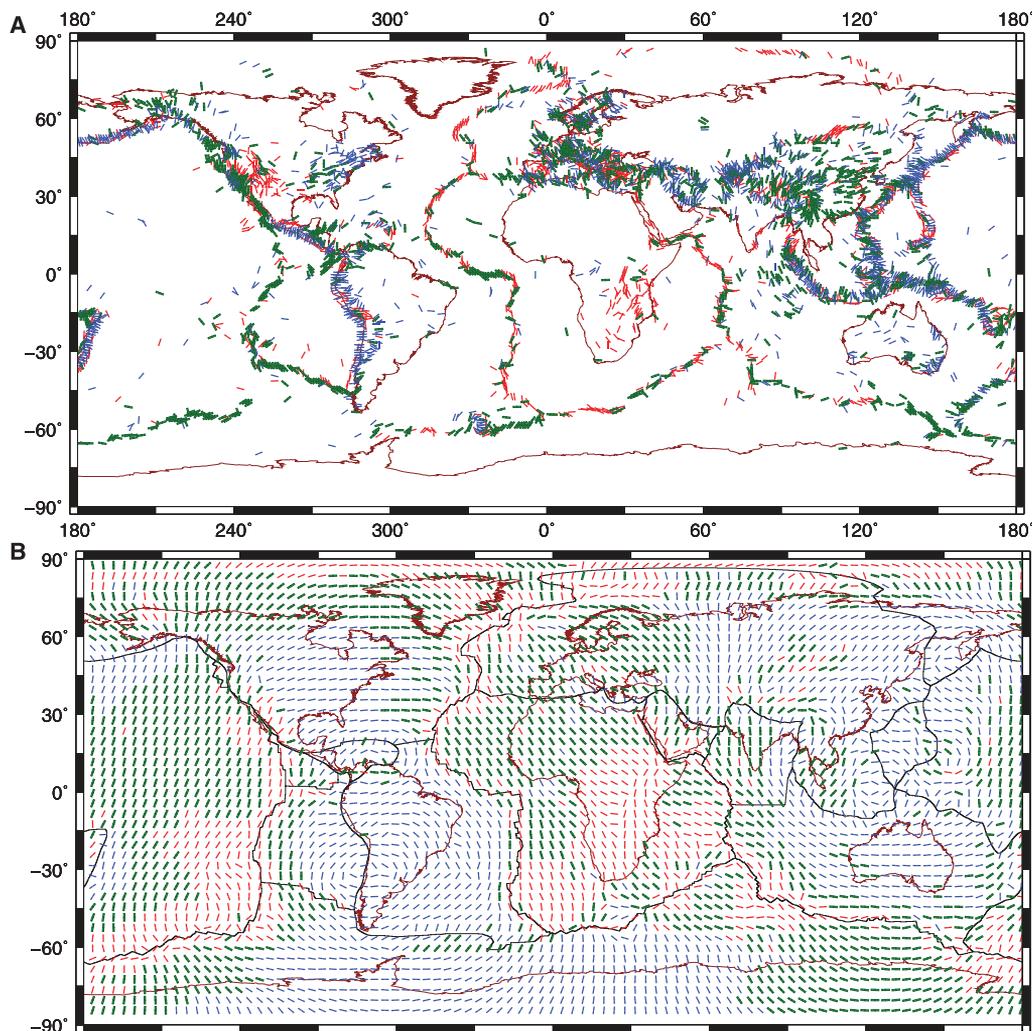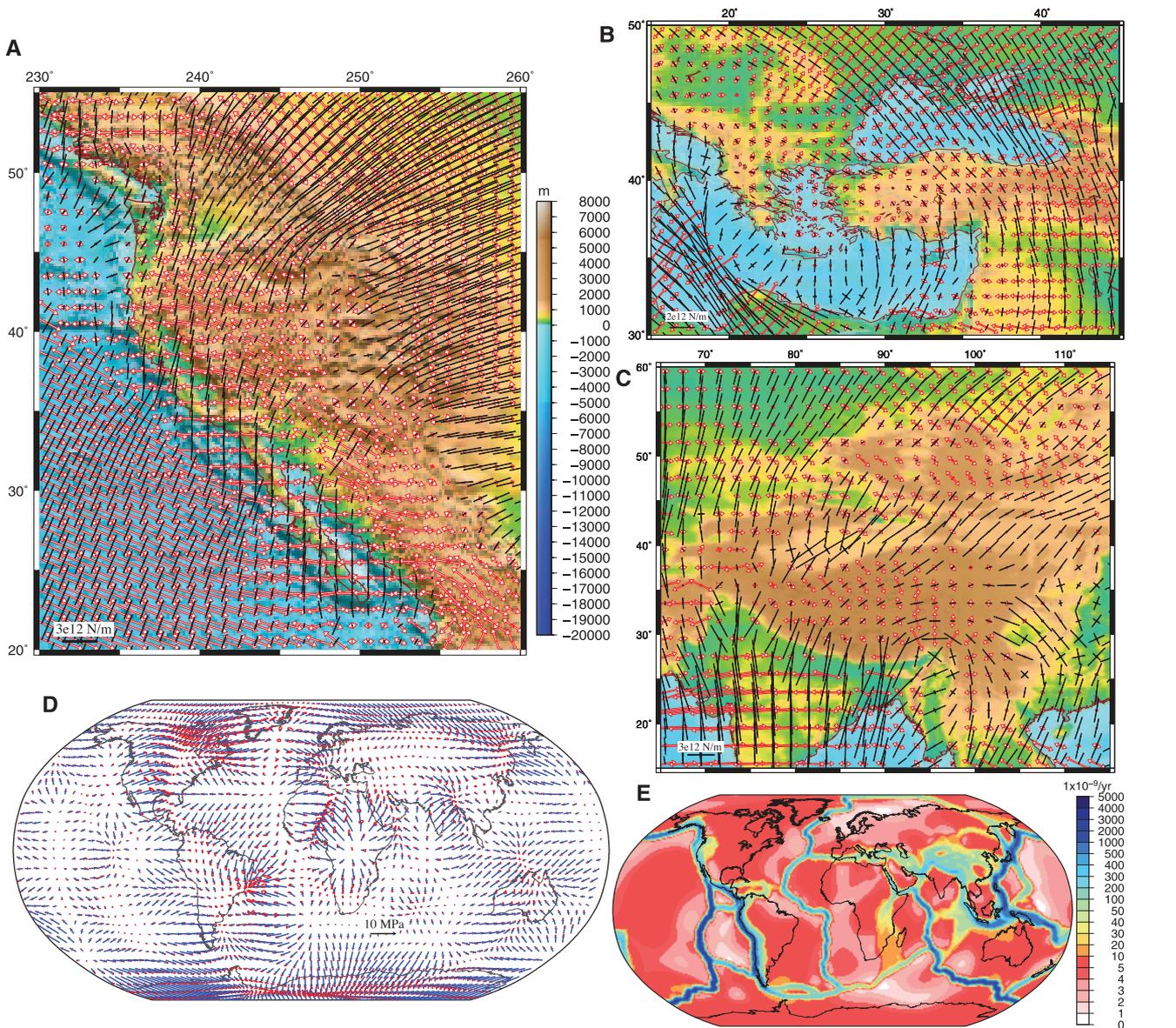
Fig. 4. (A) Deviatoric stress prediction in western North America plotted on top of topography. Red denotes tensional stresses, whereas black denotes compressive stresses. **(B)** Same as in (A), but in the central Mediterranean. **(C)** Same as in (A), but in the India-Asia collision zone. **(D)** Average horizontal tractions at the reference-level depth of 100 km below sea level, along with 95% confidence error ellipses, derived from nine mantle-flow models that fit the observations. The nine models possessed the narrow range of acceptable lateral viscosity variations described in the text and in (9). **(E)** Predicted second invariant of strain rates from our best-fitting dynamic model.

References and Notes
1. C. Lithgow-Bertelloni, J. H. Guynn, *J. Geophys. Res.* **109**, B01408 (2004).
2. P. Bird, Z. Liu, W. K. Rucker, *J. Geophys. Res.* **113**, B11406 (2008).
3. Y. Ricard, C. Vigny, *J. Geophys. Res.* **94**, 17543 (1989).
4. C. Lithgow-Bertelloni, M. Richards, *Geophys. Res. Lett.* **22**, 1317 (1995).
5. T. W. Becker, R. J. O'Connell, *Geochem. Geophys. Geosyst.* **2**, 2001GC000171 (2001).
6. B. Steinberger, H. Schmeling, G. Marquart, *Earth Planet. Sci. Lett.* **186**, 75 (2001).
7. A. Forte, R. Moucha, N. Simmons, S. Grand, J. Mitrovica, *Tectonophysics* **481**, 3 (2010).
8. G. Stadler *et al.*, *Science* **329**, 1033 (2010).
9. Methods are available as supporting material on *Science* Online.
10. A. Ghosh, W. E. Holt, L. Wen, A. J. Haines, L. M. Flesch, *Geophys. Res. Lett.* **35**, L16309 (2008).

11. C. Kreemer, D. A. Lavallée, G. Blewitt, W. E. Holt, *Geophys. Res. Lett.* **33**, L17306 (2006).
12. D. F. Argus, R. G. Gordon, C. DeMets, *Geochem. Geophys. Geosyst.* **12**, Q11001 (2011).
13. C. DeMets, R. G. Gordon, D. F. Argus, *Geophys. J. Int.* **181**, 1 (2010).
14. P. Bird, *J. Geophys. Res.* **103**, 10115 (1998).
15. A. Ghosh, W. E. Holt, L. M. Flesch, A. J. Haines, *Geology* **34**, 321 (2006).
16. O. Heidbach *et al.*, *The World Stress Map Database Release 2008* (GFZ, Potsdam, Germany, 2008).
17. S. M. Özeren, W. E. Holt, *Geophys. J. Int.* **183**, 1165 (2010).
18. C. Faccenna, T. W. Becker, *Nature* **465**, 602 (2010).
19. C. Kreemer, W. E. Holt, A. J. Haines, *Geophys. J. Int.* **154**, 8 (2003).
20. A. Ghosh, W. E. Holt, L. M. Flesch, *Geophys. J. Int.* **179**, 787 (2009).

21. By tractions we mean $-\tau_{r\theta}$ and $-\tau_{r\phi}$, which are the effective force per unit area imposed on the base of the lithosphere by mantle flow.
22. R. M. Richardson, S. Solomon, N. Sleep, *Rev. Geophys.* **17**, 981 (1979).
23. W. Bai, C. Vigny, Y. Ricard, C. Froidevaux, *J. Geophys. Res.* **97**, 11729 (1992).
24. W. C. Tao, R. J. O'Connell, *Nature* **361**, 626 (1993).
25. L. N. Moresi, M. Gurnis, *Earth Planet. Sci. Lett.* **138**, 15 (1996).
26. S. L. Bilek, C. P. Conrad, C. Lithgow-Bertelloni, *Geophys. Res. Lett.* **32**, L14305 (2005).
27. M. A. Jadamec, M. I. Billen, *Nature* **465**, 338 (2010).
28. M. I. Billen, *Annu. Rev. Earth Planet. Sci.* **36**, 325 (2008).

Cyanophora paradoxa Genome Elucidates Origin of Photosynthesis in Algae and Plants

Dana C. Price,[1] Cheong Xin Chan,[1]* Hwan Su Yoon,[2,3] Eun Chan Yang,[2] Huan Qiu,[2] Andreas P. M. Weber,[4] Rainer Schwacke,[5] Jeferson Gross,[1] Nicolas A. Blouin,[6] Chris Lane,[6] Adrián Reyes-Prieto,[7] Dion G. Durnford,[8] Jonathan A. D. Neilson,[8] B. Franz Lang,[9] Gertraud Burger,[9] Jürgen M. Steiner,[10] Wolfgang Löffelhardt,[11] Jonathan E. Meuser,[12] Matthew C. Posewitz,[13] Steven Ball,[14] Maria Cecilia Arias,[14] Bernard Henrissat,[15] Pedro M. Coutinho,[15] Stefan A. Rensing,[16,17,18] Aikaterini Symeonidi,[16,17] Harshavardhan Doddapaneni,[19] Beverley R. Green,[20] Veeran D. Rajah,[1] Jeffrey Boore,[21,22] Debashish Bhattacharya[1]†

The primary endosymbiotic origin of the plastid in eukaryotes more than 1 billion years ago led to the evolution of algae and plants. We analyzed draft genome and transcriptome data from the basally diverging alga *Cyanophora paradoxa* and provide evidence for a single origin of the primary plastid in the eukaryote supergroup Plantae. *C. paradoxa* retains ancestral features of starch biosynthesis, fermentation, and plastid protein translocation common to plants and algae but lacks typical eukaryotic light-harvesting complex proteins. Traces of an ancient link to parasites such as Chlamydiae were found in the genomes of *C. paradoxa* and other Plantae. Apparently, *Chlamydia*-like bacteria donated genes that allow export of photosynthate from the plastid and its polymerization into storage polysaccharide in the cytosol.

Eukaryote evolution has largely been shaped by the process of primary endosymbiosis, whereby bacterial cells were taken up and over time evolved into double membrane–bound organelles, the plastid and the mitochondrion [e.g., (1, 2)]. The cyanobacterium-derived plastid is found in diverse photosynthetic organisms, including Glaucophyta, Rhodophyta, and green algae and their land plant descendants (the Viridiplantae). These three lineages are postulated to form the monophyletic group Plantae (or Archaeplastida) (3–6), a hypothesis that suggests the primary cyanobacterial endosymbiosis occurred exclusively in their single common ancestor. Plastid gene trees demonstrate a single origin of the Plantae (5, 7); however, many nuclear, multiprotein phylogenies provide little (8) or no support (9, 10) for their monophyly. These latter results may reflect a reticulate ancestry among genes that can mislead phylogenetic inference (11). Furthermore, glaucophytes retain ancestral cyanobacterial features not found in other Plantae (12)—such as the presence of peptidoglycan between the two bounding membranes of the plastid (13)—that cast doubt on their evolutionary history. It is therefore unclear whether the Plantae host and its plastid, with its associated complex machinery (e.g., for plastid protein import and solute transport) (14, 15), had a single origin or multiple origins. To elucidate the evolutionary history of key algal and land plant traits and to

test Plantae monophyly, we have generated a draft assembly of the ≈70 Mbp nuclear genome from the glaucophyte *Cyanophora paradoxa* CCMP329 (Pringsheim strain) (Fig. 1A).

A total of 27,921 *C. paradoxa* proteins were predicted from the genome data, and 4628 had significant BLASTp hits ($e \leq 10^{-10}$) to prokaryote and eukaryote genome data in our comprehensive local database (table S1). Using phylogenomics (16), we generated 4445 maximum likelihood trees from the *C. paradoxa* proteins and found that >60% support a sister-group relationship between glaucophytes and red and/or green algae with a bootstrap value ≥90% (Fig. 1B and fig. S1). The Plantae clade in many of these trees is, however, interrupted by chlorophyll $a + c$ containing "chromalveolates." An example of this type of tree is fructose-1,6-bisphosphatase (Fig. 1C and fig. S2), which has cytosolic and plastidic isoforms. The gene for this enzyme, found in stramenopiles (e.g., diatoms) and haptophytes, originated from the red algal secondary endosymbiont that gave rise to the plastid in these taxa (2, 9). This sort of intracellular gene transfer associated with endosymbiosis (EGT) has greatly enriched algal and land plant genomes (17, 18).

We estimated the "footprint" of cyanobacterium-derived EGT in Plantae genomes. The proportion of cyanobacterium-derived nuclear genes varies from 18% in *Arabidopsis thaliana* (19) to ~7% in mesophilic red algae and 6% in *Chlamydomonas*

reinhardtii (20, 21). Phylogenomic analysis of the predicted *C. paradoxa* proteins showed 274 to be of cyanobacterial provenance (22). This constitutes ~6% of proteins in the glaucophyte that have significant BLASTp hits (i.e., 274 out of 4628), as found in other algae (20, 21). BLASTp analysis identified 2029 proteins that are putatively destined for the plastid, of which 293 contain the transit sequence for plastid import [identified by the presence of phenylalanine (F) within the first four amino acids: MF, MAF, MNAF, MSAF, and MAAF] (23, 24) (fig. S4B). Of these 293 proteins, 80% are derived from Cyanobacteria.

Another source of foreign genes in Plantae is horizontal gene transfer (HGT), which is not associated with endosymbiosis. Using 35,126 bacterial sequences as a query, we found 444 noncyanobacterial gene families with a common origin shared amongst Bacteria and Plantae. Among them, 15 genes are present in all three Plantae phyla. An example of a gene derived from Bacteria after an ancient HGT event that is shared by

[1]Department of Ecology, Evolution and Natural Resources and Institute of Marine and Coastal Sciences, Rutgers University, New Brunswick, NJ 08901, USA. [2]Bigelow Laboratory for Ocean Sciences, West Boothbay Harbor, ME 04575, USA. [3]Department of Biological Sciences, Sungkyunkwan University, Suwon 440-746, Korea. [4]Institute for Plant Biochemistry, Heinrich-Heine-University, D-40225 Duesseldorf, Germany. [5]Botanical Institute, Biocenter Cologne, University of Cologne, Zülpicher Strasse 47b, 50674 Cologne, Germany. [6]Department of Biological Sciences, University of Rhode Island, Kingston, RI 02881, USA. [7]Canadian Institute for Advanced Research, Department of Biology, University of New Brunswick, Fredericton, New Brunswick E3B 5A3, Canada. [8]Department of Biology, University of New Brunswick, Fredericton, New Brunswick E3B 5A3, Canada. [9]Centre Robert Cedergren, Département de Biochimie, Université de Montréal, Montréal, Québec H3C 3J7, Canada. [10]Department of Biology/Plant Physiology, Martin-Luther-University Halle-Wittenberg, Germany. [11]Max F. Perutz Laboratories, Department of Biochemistry and Cell Biology, University of Vienna, Vienna, Austria. [12]Department of Civil and Environmental Engineering, Colorado School of Mines, Golden, CO 80401, USA. [13]Department of Chemistry and Geochemistry, Colorado School of Mines, Golden, CO 80401, USA. [14]Unité de Glycobiologie Structurale et Fonctionnelle, UMR 8576 CNRS-USTL, Université des Sciences et Technologies de Lille, 59655 Villeneuve d'Ascq Cedex, France. [15]Universités Aix-Marseille I & II, Case 932, 163 Avenue de Luminy, 13288 Marseille Cedex 9, France. [16]Faculty of Biology, University of Freiburg, Freiburg, Germany. [17]FRISYS Freiburg Initiative in Systems Biology, University of Freiburg, Freiburg, Germany. [18]BIOSS Centre for Biological Signalling Studies, University of Freiburg, Freiburg, Germany. [19]Roy J. Carver Center for Genomics, Department of Biology, University of Iowa, Iowa City, IA, 52242, USA. [20]Department of Botany, University of British Columbia, Vancouver, British Columbia V6T 1Z4, Canada. [21]Genome Project Solutions, Hercules, CA 94547, USA. [22]Department of Integrative Biology, University of California, Berkeley, CA 94720, USA.

*Present address: Institute for Molecular Bioscience, University of Queensland, Brisbane, QLD 4072, Australia.
†To whom correspondence should be addressed. E-mail: bhattacharya@aesop.rutgers.edu